



Enhancing optical absorption and charge transfer: Synthesis of S-doped *h*-BN with tunable band structures for metal-free visible-light-driven photocatalysis



Chengyang Feng^{a,b,*}, Lin Tang^{a,b,*}, Yaocheng Deng^c, Guangming Zeng^{a,b,*}, Jiajia Wang^{a,b}, Yani Liu^{a,b}, Zhaoming Chen^{a,b}, Jiangfang Yu^{a,b}, Jingjing Wang^{a,b}

^a College of Environmental Science and Engineering, Hunan University, Changsha, 410082, China

^b Key Laboratory of Environmental Biology and Pollution Control, Hunan University, Ministry of Education, Changsha, 410082, China

^c College of Resources and Environment, Hunan Agricultural University, Changsha, 410028, China

ARTICLE INFO

Keywords:

Hexagonal boron nitride
Two-dimensional material
Band structure regulation
Interlayer compaction
Photocatalysts

ABSTRACT

Two-dimensional materials, especially metal-free two-dimensional materials such as graphene, carbon nitride and boron nitride have attracted significant attention for photocatalysis technology due to their unique charge mobility. Herein, S-doped *h*-BN with tunable band structure and layer stacking distance has been developed via a facile heat treatment strategy. Compared to the pristine *h*-BN, the optimized S-doped *h*-BN exhibited enhanced optical absorption, charge transfer, surface reactivity and hydrophilicity, which greatly improved its ability for photocatalytic degradation of 2,4-DCP. It is clearly demonstrated, by means of various experiments and characterizations, that the bandgap and layer spacing of *h*-BN can be adjusted by controlling the S doping amount. DFT calculations exposed that the p-orbitals and d-orbitals from sulfur are involved in the formation of the new valence and conduction band edges, which gradually reduced the CB potential, narrowed the bandgap and enhanced the optical absorption property of *h*-BN. And the shortened layer stacking distance and abundant S doping sites may be the main reason for the promotion of charge mobility and surface reactivity. Through this strategy, *h*-BN was vested with the ability of visible light response, which provides insights for the modification of other semiconductor materials with wide bandgap, and the study on the compression compaction phenomenon of interlayer stacking distance can open up a new feasible route to enhance charge mobility of other two-dimensional semiconductor materials.

1. Introduction

Facing the present energy and environmental challenges, it is imperative to develop clean and renewable energy. Solar energy, the most promising renewable energy sources, is the focus of current and future research and development [1–4]. Photocatalysis can convert solar energy into chemical energy, which is an important development direction of solar energy capture technology. Recently, two-dimensional (2D) semiconductor materials have received great attention in the fields of photocatalysis [5–9], electrocatalysis [10,11], solar cells [12,13] and photodetectors [14,15] due to their unique structural and electronic properties. In particular, a large number of 2D materials, such as graphene, graphitic carbon nitride and transition metal dichalcogenides, have been used as photocatalysts and achieved superior performance [16–20]. However, 2D materials are usually assembled into bulk by van

der Waals forces between layers, and then the photogenerated charges excited inside materials need to cross the layer space to get to the surface. And the barrier effect of layer stacking structure on photogenerated charge migration is one of the major factors limiting the photocatalytic activities of 2D materials. Therefore, multiple approaches have been developed to improve this problem, such as exfoliation of the materials into ultra-thin or even single-layer to reduce the layers of charge migration [21,22], construction of porous structure to expose the interior of materials [23–25], and compaction of the interlayer stacking distance to improve charge transfer efficiency [26,27].

Hexagonal boron nitride (*h*-BN), a novel 2D material with similar structure to graphene, is a promising metal-free photocatalyst which has been applied in many applications including organic pollutant degradation [28–32], hydrogen production [33–37], and CO₂ reduction [38,39]. The excellent chemical and thermal stability, environmental

* Corresponding authors at: College of Environmental Science and Engineering, Hunan University, Changsha, 410082, China.

E-mail addresses: tanglin@hnu.edu.cn (L. Tang), zgming@hnu.edu.cn (G. Zeng).

friendliness and high specific surface area are the main factors for its gaining wide attention in the field of photocatalysis. However, the light response range of *h*-BN is limited to ultraviolet region due to its wide bandgap, restricting the solar energy utilization. On the other hand, its poor dispersion in water does not favor the reaction in liquid phase. And, similar to most 2D stacking materials, the photogenerated charges excited inside the *h*-BN are hard to migrate to the surface, which results in serious electron-hole recombination and inferior charge utilization. Although some methods [33,40,41] have been developed to improve the photocatalytic performance of *h*-BN, it is still a great challenge to develop a facile method to solve the existing problems.

h-BN owns wide bandgap as N 2p and B 2p orbitals form its valence and conduction band, respectively. It was revealed by the first-principle calculations that the doping of sulfur can significantly reduce the bandgap of *h*-BN, and the S 3d orbitals can form intermediate states and reduce the energy required for photoelectron transition. Herein, the sulfur doping of *h*-BN would be a good strategy to optimize the optical absorption capacity. In this work, for the first time, a facile two-step thermal treatment strategy was described to prepare sulfur doping *h*-BN. The introduction of sulfur exhibited a redshift in the absorption edge of *h*-BN, and the shift size can be controlled by sulfur doping. More interestingly, XRD and HRTEM showed that the interlayer stacking distance of *h*-BN was compacted after doping with sulfur, which could be attributed to the increased interlayer interaction caused by the large amount of polar B-S bonds. Owing to the redshift of absorption edge and compaction of interlayer stacking distance, the prepared *h*-BN exhibited enhanced optical absorption and charge transfer ability. And a well-designed photocurrent experiment disclosed that S-BN possesses enhanced surface charge transfer efficiency than pristine *h*-BN, which may be due to the formation of more surface active sites after doping. The photocatalytic performances of prepared samples were evaluated by the degradation of 2,4-dichlorophenol (2,4-DCP) under UV and visible light irradiation. The S-doped *h*-BN photocatalysts exhibited excellent removal efficiency of 2,4-DCP under both UV and visible light, while the pristine *h*-BN samples only showed photocatalytic performance under UV light, indicating the success and validity of the modification strategy in this work. The synthetic strategy presented here thus put forward a simple way of synergistically optimizing the optical absorption, charge transfer and surface reactivity of *h*-BN based materials.

2. Experimental section

2.1. Materials

All chemical reagents were analytical grade and used without further purification. Boric acid, urea, sublimed sulfur, 2,4-dichlorophenol (2,4-DCP), isopropanol (IPA), ethylenediaminetetraacetic acid disodium (EDTA-2Na) and 1,4-benzoquinone (BQ) were purchased from Sinopharm Chemical Reagent Co., Ltd (Shanghai China). Deionized water was produced by an ultrapure laboratory water system and used in the whole experiment.

2.2. Samples preparations

Hexagonal boron nitride (*h*-BN) was synthesized by calcination using boric acid and urea. Typically, 2.0 g boric acid and 8.0 g urea were co-dissolved in 50 mL deionized water to form a clear solution. The mixed solution was transferred into vacuum oven at 60 °C until volatilization of water. Then the obtained gels were transferred into a quartz boat and heated to 900 °C with a heating rate of 4 °C/min and kept at 900 °C for 5 h under nitrogen atmosphere. After cooling to room temperature, the white *h*-BN product was collected and ground into powders.

The sulfur doped *h*-BN (S-BN) was prepared by a simple heat treatment. In a typical synthesis process, 1 g obtained *h*-BN powders

and 0.2 g of sublimed sulfur were ground and mixed fully. Then the mixture was transferred into a horizontal tube furnace and heated to 440 °C with a heating rate of 5 °C/min under nitrogen atmosphere, and kept at this temperature for a certain time (30, 60, 90, 120 min). Next the temperature was increased to 500 °C and continued to heat the sample for another 2 h to remove the unreacted S. The final taupe powders were obtained after washing with ethanol and water for several times and dried at 60 °C for 12 h. The obtained sample was labeled as xS-BN, when x is 1, 2, 3 and 4, the heating time at 400 °C is 30, 60, 90 and 120 min, respectively.

2.3. Characterization of samples

The phase structures of as-prepared samples were studied by X-ray diffractometry (XRD) measurement on a Bruker AXS D8 Advance X-ray diffractometer with Cu-K α irradiation (40 kV/40 mA). The morphologies and microstructures were investigated by a F20 S-TWIN transmission electron microscopy (TEM, Tecnai G2, FEI Co). The thermogravimetric analysis (TGA) of samples was measured by a thermo gravimetric analyzer (Q500, TA Instruments) under N₂ atmosphere. The Fourier transform infrared spectroscopy (FT-IR) was measured on a NICOLET iN10 spectrometer. The surface chemical compositions were analyzed by X-ray photoelectron spectroscopy (XPS, ESCALAB 250Xi, Thermo Fisher). The diffuse reflectance absorption spectra (DRS) of samples were measured by a UV-vis spectrophotometer (Cary 300, USA) with an integrating sphere attachment and BaSO₄ reference. The photoluminescence (PL) spectroscopy was measured by a Fluoromax-4 spectrophotometer at room temperature. The time-resolved transient PL decay of samples was measured by a FLS980 Series of Fluorescence Spectrometers with an excitation wavelength of 320 nm at room temperature. The specific surface areas of samples were characterized via a nitrogen adsorption-desorption and Brunauer-Emmett-Teller (BET) method by a surface area analyzer (NOVA 2200E, Quantachrome).

2.4. Photoelectrochemical measurements

The electrochemical and photoelectrochemical measurements were recorded by a CHI 660D workstation in a three-electrode cell. A Pt electrode and an Ag/AgCl electrode were used as the counter and reference electrode, respectively. A FTO (active area of 1 cm²) electrode covered with samples was used as the working electrode. A 300 W Xe lamp was used as light source. The transient photocurrent response, open circuit potential (OCP), current-voltage (J-V) and impedance-potential curves of samples were measured with 0.2 M Na₂SO₄ electrolyte solution, and the electrochemical impedance spectroscopy (EIS) of samples were measured with phosphate buffer (pH = 7.4) containing 5 mM ferro/ferricyanide and 20 mM KCl.

2.5. Photocatalytic degradation test

The photocatalytic degradation activity of prepared samples was investigated by the degradation of 2,4-dichlorophenol (2,4-DCP) under UV and visible light irradiation. A 300 W Xe lamp with different wavelength cutoff filters was used as light source. In a typical procedure, 20 mg sample was mixed with 50 mL 2,4-DCP solution (10 mg/L) and stirred for 30 min in the dark to achieve the adsorption-desorption equilibrium. The reaction system was exposed to the 300 W Xe lamp with continues stir. The reaction solution was collected and analyzed by UV-vis spectrophotometer every 20 min.

To investigate the active species in the degradation process, ethylenediaminetetraacetic acid disodium (EDTA-2Na), isopropanol (IPA) and 1,4-benzoquinone (BQ) were chosen as scavengers for holes (h⁺), hydroxyl radical (·OH) and superoxide radical (·O₂⁻), respectively. Typically, 20 mg samples with different scavengers (1 mmol) were dispersed in 50 mL 2,4-DCP solution (10 mg/L), and the following processes are similar to the photocatalytic degradation experiments.

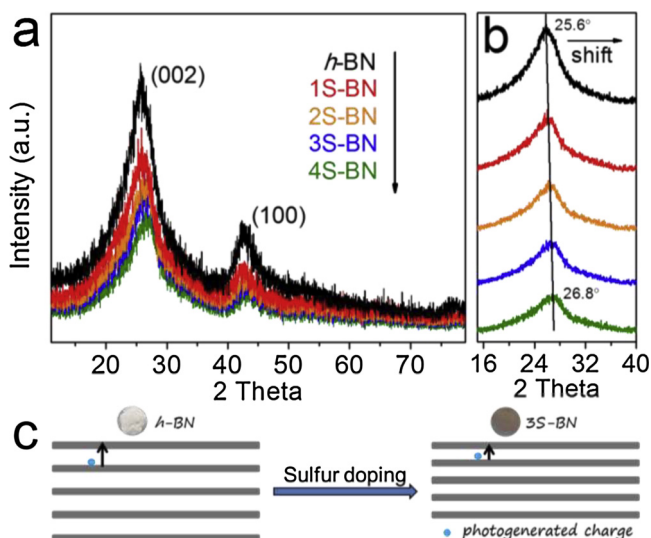


Fig. 1. (a) Powder XRD patterns of *h*-BN and xS-BN. (b) The local contrast of XRD patterns for *h*-BN and xS-BN around (002) peak. (c) Scheme for the proposed interlayer charge transfer of *h*-BN and S-BN.

2.6. Theoretical calculations

The first-principles calculations were performed within the framework of DFT as implemented in the Vienna Ab-initio Simulation Package (VASP). The exchange-correlation interactions were treated by generalized gradient approximation (GGA) parameterized by Perdew, Burke, and Ernzerhof (PBE). The interaction between ions and electrons was described using the projected augmented wave (PAW) formalism with an energy cutoff of 400 eV. All the structures were fully relaxed until the force on each atom was less than 0.01 eV/Å. The Gaussian smearing was used with a smearing width of 0.2 eV. The Brillouin zone integrations were performed using Monkhorst-Pack scheme with $2 \times 2 \times 6$ k-point meshes.

3. Results and discussions

The chemical structure and layered-stacking distance of as-prepared samples were first characterized by X-ray diffraction (XRD) patterns. As shown in Fig. 1a, *h*-BN shows two distinct peaks located at 25.7° and 42.4°, corresponding to the (002) and (100) crystal planes. Typically, the (002) and (100) planes represent the interlayer stacking and in-plane packing of *h*-BN [42], respectively. It is obvious that the (002) peak shifts from 25.7° to 26.8° with the sulfur doping amount increases (Fig. 1b), revealing that the interlayer stacking distances was compacted, and the compaction degree was related to the doping amount. The increased interlayer van der Waals attraction which arose from the polar B-S bonds could be the cause of the compaction of stacking distance. The (100) peak also shifts to higher 2 theta angles with increasing sulfur doping, and its intensity decreases obviously, indicating the structural changes of in-plane packing. A simplified model of stacking state is demonstrated in Fig. 1c, obviously, the path length decreases for internal electrons to move to the surface after interlayer compaction, which not only promotes the charge transfer but also reduces the energy loss [26,27,43]. To further study the change of interlayer stacking distance, TEM was used to characterize the prepared samples visually. As shown in Fig. 2 and Figure S1, the morphologies of *h*-BN and xS-BN are basically the same, and the SEM images (Figure S2) also show that both *h*-BN and S-doped *h*-BN samples revealed a nanosheet structure, indicating the introduction of sulfur didn't destroy the morphology of *h*-BN. The selected area electron diffraction (SAED) pattern verified the amorphous nature of *h*-BN (Figure S3). The typical layer stacking structure (the 002 planes) can be clearly observed in the

HRTEM images (Fig. 2c, h and Figure S1 c, g), and the interlayer distances were measured along the dotted line and shown in Fig. 2d, i and Figure S1 d, h. The interlayer distances of *h*-BN, 1S-BN, 2S-BN and 3S-BN were calculated to be 0.364, 0.358, 0.353 and 0.347 nm, respectively, which shows the same trend as the XRD tests. The EDS analysis (Fig. 2e, j) revealed that S-BN contains sulfur but *h*-BN does not, suggesting the layer compaction was related to the sulfur doping.

Element mapping of S-BN (Figure S4) shows a uniform distribution of B, N and S throughout the whole selected area, confirming the uniform doping of sulfur in *h*-BN. The excellent thermostability of *h*-BN and S-BN was confirmed by TGA (Figure S5a) that there was no significant weight loss even at 800 °C. The TGA curves shows that the weight of S-BN remained constant after 200 °C, given that the boiling point of elemental sulfur was about 444.6 °C. It can be determined that the S elements in S-BN were not deposited through physical adsorption, but chemically combined. Figure S6 displays the FT-IR spectra of *h*-BN and S-BN samples. Two strong peaks at 797 and 1352 cm⁻¹ corresponded to the B-N-B and B-N band in *h*-BN. After the doping of sulfur, a slight blueshift and redshift can be observed at the B-N-B and B-N bond, respectively, confirming the successful bonding of sulfur in *h*-BN. The elemental compositions and chemical states of *h*-BN and S-BN samples were further characterized by X-ray photoemission spectroscopy (XPS) and shown in Figure S5. XPS survey spectra (Figure S5b) reveal that these samples mainly consist of B, N and O elements, and the characteristic peaks of S can just be observed in the high resolution XPS spectra of S-BN (Figure S5e). The high consistent C 1s peaks at 284.74 eV are related to the carbon containing substances attached on the surface of samples. For the pristine *h*-BN, the high resolution of B 1s and N 1s spectra both show main characteristic peaks of sp³ hybridized B-N bonds located at 190.69 eV and 389.14 eV, respectively. The subordinate peak in B 1s spectrum (Figure S5c) belongs to B-O bonds coming from the boric acid precursor and existing in *h*-BN network. And for S-BN, the B-O peak shifts to a low binding energy, indicating the chemical states of B changed after the introduction of S. On the other hand, the N 1s spectrum of S-BN is almost unchanged compared to *h*-BN (Figure S5d), which suggests that the doped S had no effect on the chemical states of N. Hence, it is plausible to extrapolate that the doped S were bound to B.

The effect of S doping on the optical response of *h*-BN was first tested by photocurrent transient response experiments. Figure S7a shows the photocurrent density curves of *h*-BN and xS-BN samples under UV light irradiation. The pristine *h*-BN exhibits the weakest photocurrent density due to its poor light absorption performance and serious charge recombination, and obviously, the photocurrent intensities of 1S-BN, 2S-BN and 3S-BN increase successively with the increase of S doping, indicating the introduction of S can effectively regulate the optical response of *h*-BN within a certain range. However, for 4S-BN, although the range of light absorption is larger, the photocurrent intensity decreases compared to 2S-BN and 3S-BN, which may be attributed to the excessive S that destroyed the structure of *h*-BN. The change of in-plane unit structure has been confirmed by the XRD patterns (Fig. 1a) where the (100) peak decreased significantly with the S doping, preventing the transfer of photoexcited charges and causes the reduced photocurrent. Under visible light irradiation (Figure S7b), the pristine *h*-BN cannot show the electrical signal response due to its wide bandgap (3.93 eV), and the obvious photocurrent of xS-BN indicates that the doping of S can extend the light response range to the visible region. Meanwhile, the photocatalytic performance of *h*-BN and xS-BN samples were measured by the degradation of 2,4-DCP under UV light irradiation. As shown in Figure S8, xS-BN samples exhibited enhanced photocatalytic degradation activity compared with pure *h*-BN, and the 3S-BN showed the best performance, which was the same as the result of photocurrent response experiment. Given that 3S-BN exhibited the best optical response capability and photocatalytic performance, 3S-BN was used as the optimal catalyst in the following study and marked as S-BN. To further investigate the optical absorption and band

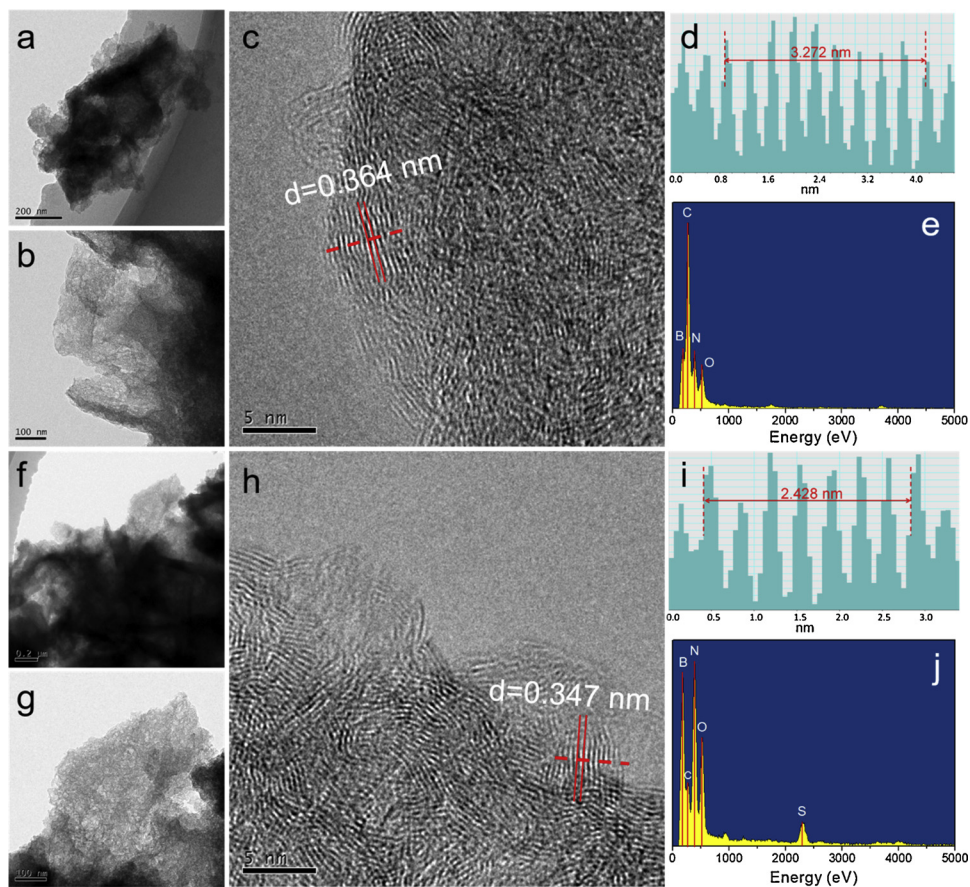


Fig. 2. (a, b) TEM and (c) HR-TEM images of *h*-BN. (d) Intensity profiles along the dotted line indicated in image (c). (e) EDS analysis of *h*-BN; (f, g) TEM and (h) HR-TEM images of 3S-BN. (i) Intensity profiles along the dotted line indicated in image (h). (j) EDS analysis of 3S-BN.

structure of prepared *h*-BN and xS-BN samples, the UV-vis diffuse reflectance spectroscopy (DRS) were measured and shown in Fig. 3a. A significant redshift in the absorption edge was achieved with increasing S doping, indicating the reduction of the bandgap. Furthermore, the absorbance of xS-BN in the UV region is also greatly promoted, the co-improvement of optical absorption range and absorptivity can enhance the light utilization more effectively. The bandgaps of samples were determined from the transformed Kubelka-Munk function [44,45] and shown in Fig. 3b. With the increase of S doping, bandgaps of *h*-BN and xS-BN narrow from 3.93 to 2.77 eV. The electrochemical flat-band potentials (E_{fb}) of prepared samples were determined by Mott-Schottky analysis [46]. The Mott-Schottky plots of all samples under different frequencies with positive slope linear region are shown in Figure S9, indicating the n-type nature of samples. The calculated E_{fb} values of *h*-BN and xS-BN are compared in Fig. 3c, and clearly, the E_{fb} positive shifts gradually with the increase of S content. Since the E_{fb} of an n-type semiconductor is close to its CB potential (≈ 0.2 V below the CB), it can be inferred that the CB positions of *h*-BN, 1S-BN, 2S-BN, 3S-BN and 4S-BN decrease successively. However, the VB XPS spectra (Fig. 3d) suggested that the VB position of samples was almost unaffected by the introduction of S, indicating that the doped S mainly changed the CB of *h*-BN but had little influence on the VB.

To further understand the relationship between doped S and the narrowed bandgaps of xS-BN, the density-functional theory (DFT) calculations of the band structure and partial density of states (PDOS) were performed (Figure S10). The calculated results of band structures show that some new orbitals energy levels appear on the CB and result in the descent of CB position, while the VB position have barely budged. And the intrinsic bandgap of *h*-BN decreases with the increase of S doping concentration, which agrees well with the change trend of the

experimental phenomena above. The PDOS results further reveal the influence of S on the bandgap narrowing. As illustrated in Figure S10, both the p-orbitals of B and N contribute to the CB of *h*-BN, while the VB is mainly composed of p-orbitals of N. After the introduction of S, the d-orbitals of S atoms participate in the composition of VB and lower it. However, although the p-orbitals of S atoms are involved in the formation of VB, they have little influence on the position of VB. Compared with the PDOS pattern of each element, the total PDOS pattern represents the superposition of influence of all elements in the material on the formation of band structure, which can more intuitively reflect the changes of energy bands. The total PDOS for the simulated S doping *h*-BN is shown in Fig. 3e and revealed the narrowed bandgaps with the increase of doping amount. Herein, in combination with the experimental and simulation results above, the change of bandgaps of *h*-BN and xS-BN samples are illustrated in Fig. 3f. It is clear that S-doping is an effective way to modify the electronic band structure of *h*-BN, and the narrower bandgaps of the xS-BN samples originating from the decrease in CB position can enhance the optical absorption ability and is beneficial for the carrier transfer.

In addition to increasing the optical absorption capacity of *h*-BN, the introduction of S can also influence the separation of photogenerated electrons and holes. The room temperature PL spectroscopy measurement of *h*-BN and S-BN was performed with an excitation wavelength of 250 nm and shown in Fig. 4a, where the pristine *h*-BN exhibits strong PL intensity owing to its serious charge recombination. The PL signal decreases with the doping of S, indicating the introduction of S can significantly enhance the charge separation of photoexcited charge carriers in *h*-BN. And the obvious redshift of the PL signal confirmed the bandgap decrease of S-BN. To further confirm the charge recombination inhibition, analysis of charge lifetime was performed by time-resolved

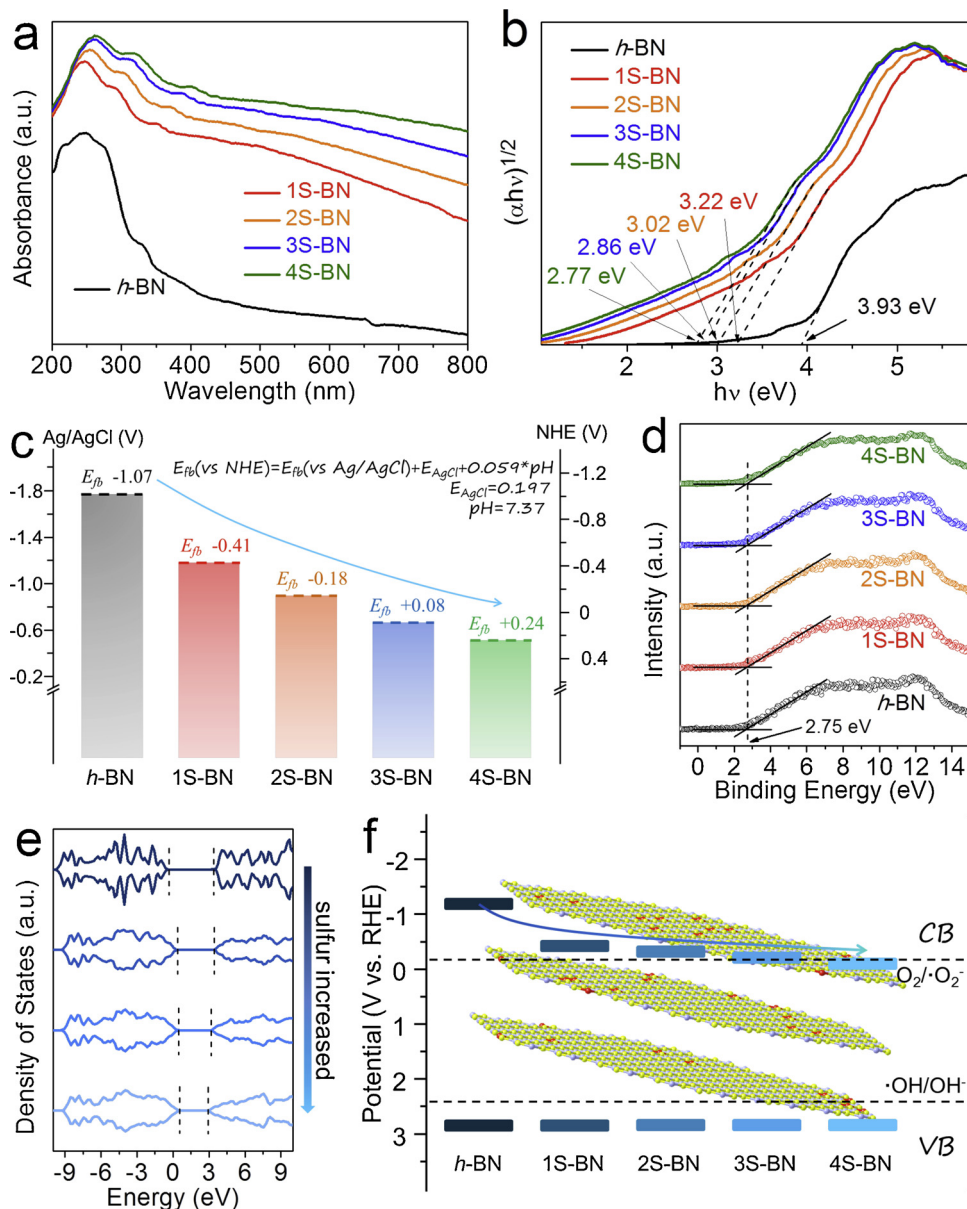


Fig. 3. (a) UV-vis DRS and (b) plots of transformed Kubelka-Munk function versus photon energy for *h*-BN and *x*S-BN samples. (c) The schematic of E_{fb} potential variations and (d) VB XPS spectra of *h*-BN and *x*S-BN samples. (e) The total PDOS for the simulated S doping *h*-BN: pure *h*-BN, 3% S doped, 6% S doped, 9% S doped. (f) The schematic diagram for the band variations of *h*-BN and *x*S-BN samples.

transient PL decay (Fig. 4b). The average emission lifetime which reflecting the emission decay process of samples was calculated by the following equation [47,48].

$$\tau_A = (A_1\tau_1^2 + A_2\tau_2^2)/(A_1\tau_1 + A_2\tau_2) \quad (1)$$

where τ_1 and τ_2 are the emission lifetime, A_1 and A_2 are the corresponding amplitudes. The calculated lifetime of *h*-BN ($\tau_{h\text{-BN}}$) and S-BN ($\tau_{S\text{-BN}}$) are 5.11 and 18.78 ns, respectively, indicating that the introduction of S can effectively promote the charge transfer and exhibit the charge recombination. The surface recombination rates of *h*-BN and S-BN were also evaluated using the normalized transient decay profile of open circuit potential (OCP) [49,50]. As shown in Fig. 4c, the open circuit potential (V_o) decayed slowly after cutting off the light source due to the recombination of photogenerated electrons and holes. The average recombination rate can be estimated by the following equation:

$$(V - V_{dark})/(V - V_{light}) = 1 - \exp(-kt) \quad (2)$$

where V , V_{dark} and V_{light} are V_o at any time, in the dark and under

illumination, k is the pseudo-first order recombination rate constant (s^{-1}). Obviously, the *h*-BN decays much slower than S-BN after light-off, and the calculated recombination rate constant of S-BN ($0.166 s^{-1}$) is about 58% as that of *h*-BN ($0.287 s^{-1}$), indicating the greatly suppressed surface recombination rate of S-BN samples. The improved charge transport of S-BN can also be confirmed by the electrochemical impedance spectroscopy (EIS). As shown in Fig. 4d, the decreased hemicycle radius of S-BN reflects the lower electric resistance, which is beneficial for the charge transport and separation. The charge conduction and optical response ability of *h*-BN and S-BN were further evaluated by measuring the current-voltage (J - V) curves under UV light irradiation with the linear sweep voltammetry (LSV) technique (Fig. 4e). The higher current density of S-BN in the dark indicates the better electrical conductivity, which benefits from the compaction of layer spacing. And obviously, when exposed to light, S-BN sample exhibits a stronger and more sensitive photocurrent response, revealing the enhanced light utilization. Therefore, the above results strongly implied that the introduction of S can help to largely improve the

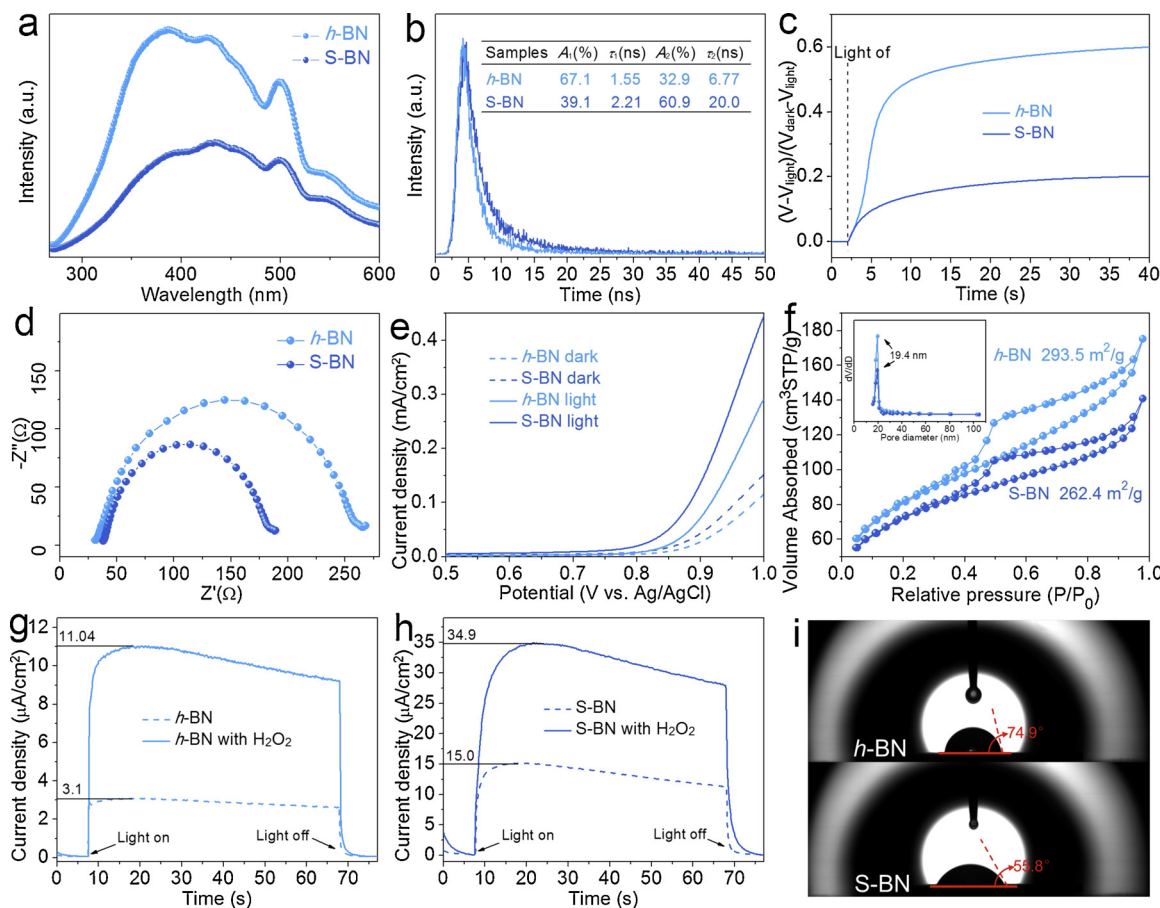


Fig. 4. (a) Photoluminescence spectra (PL), (b) time-resolved transient PL decay and (c) normalized open-circuit potential (V_o) decay curves of pristine h-BN and S-BN. (d) Electrochemical impedance spectroscopy (EIS) and (e) current-voltage (J - V) curves of pristine h-BN and S-BN. (f) Nitrogen adsorption-desorption isotherms and corresponding pore size distribution of h-BN and S-BN. Photocurrent density of (g) h-BN and (h) S-BN under UV light irradiation without and with 0.5 M H_2O_2 . (i) Static water contact-angle measurement of h-BN and S-BN.

photoactivity of h-BN.

The surface property of catalysts is one of the important factors affecting the catalytic activity. The nitrogen adsorption-desorption isotherm analysis was first used to determine the specific surface areas and pore size distribution of h-BN and S-BN (Fig. 4f). Although both h-BN and S-BN exhibit large specific surface area, the introduction of S still reduces the specific surface area of h-BN to some extent. And h-BN and S-BN show similar pore size distribution while the S-BN owns smaller pore volume. The reduced specific surface area and pore volume might be attributed to the increased density caused by the compaction of interlayer. Generally speaking, higher specific surface area and pore volume can provide more reaction sites, so the results of nitrogen adsorption-desorption isotherm analysis seem to indicate that the introduction of S is not conducive to the surface reaction of S-BN. To further investigate the surface reactivity of prepared samples, a series of elaborately designed photoelectrochemical tests [51–53] were performed to approximate the surface charge transfer efficiency (η_t). Typically, the photocurrent of h-BN and S-BN were measured in 0.2 M Na_2SO_4 aqueous solution under UV light irradiation, and meanwhile, H_2O_2 was added into the electrolyte as a fast electrons scavenger to increase the η_t . The test results are shown in Fig. 4g and h, and the photocurrent density can be defined by the following equation.

$$J_p = J_a \times \eta_s \times \eta_t \quad (3)$$

where J_p is the measured photocurrent density, J_a is the theoretical maximum photocurrent density converted by the absorbed photo energy, η_s is the charge separation efficiency, and η_t is the surface charge transfer efficiency. When enough H_2O_2 is added to electrolyte, the

surface charge transfer efficiency is greatly increased and the η_t approximately reaches 100%. Hence, the photocurrent density in the presence of H_2O_2 (J_p^{H2O2}) can be counted by following equation:

$$J_p^{H2O2} = J_a \times \eta_s \quad (4)$$

As the J_a and η_s are the intrinsic properties of h-BN and S-BN and unchanged with or without H_2O_2 , the surface charge transfer efficiency (η_t) can be counted as following equation:

$$\eta_t = J_p / J_p^{H2O2} \quad (5)$$

As shown in Fig. 4f and g, the photocurrent densities of h-BN and S-BN increase from 3.1 and 15.0 $\mu A/cm^2$ to 11.04 and 34.9 $\mu A/cm^2$, respectively, with the presence of H_2O_2 . Hence, the surface charge transfer efficiencies (η_t) of h-BN and S-BN were calculated to be 28.1% and 42.9%, respectively, indicating that S-BN possesses higher surface charge transfer efficiency than pristine h-BN. The higher surface charge transfer efficiency of S-BN seems to contradict the BET results, but this phenomenon also implies that the introduction of S can provide more surface active sites and recover the negative influence of reduced specific surface area and pore volume. Furthermore, it is widely accepted that the hydroxyl radical (OH) generated from water on the surface of photocatalyst is a very important reactive substance in photocatalytic treatment of wastewater, and the close contact between water and catalyst plays an important role in promoting the reaction of hydroxyl radical generation [24,54]. In this case, static water contact-angle measurement of h-BN and S-BN was performed to test the surface hydrophilicity and the results are displayed in Fig. 4i. The S-BN shows a contact angle of 55.8°, which is much smaller than that of pristine h-BN

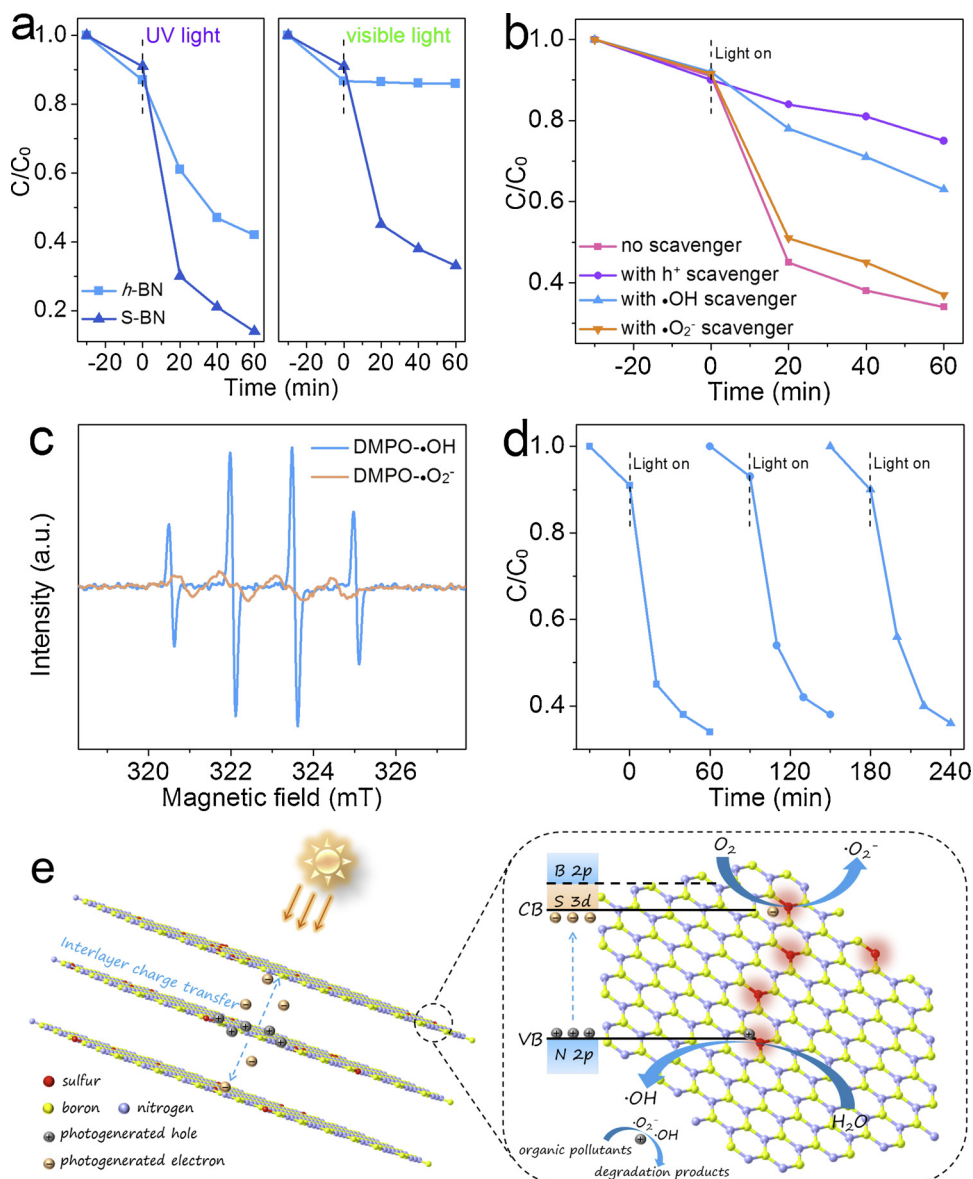


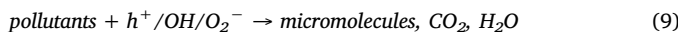
Fig. 5. (a) Photocatalytic degradation rates for 2,4-DCP over *h*-BN and S-BN under different light condition. (b) Photocatalytic degradation of 2,4-DCP over S-BN alone and with the h^+ (hole), OH and $\cdot O_2^-$ scavengers. (c) ESR signals of DMPO-OH and DMPO- $\cdot O_2^-$ under visible light. (d) Cycling runs for photocatalytic degradation of 2,4-DCP over S-BN. (e) Schematic diagram for the interlayer charge transfer, band structure change and 2,4-DCP degradation process of S-BN photocatalysts.

(74.9°), indicating the higher surface hydrophilicity of S-BN. The closer contact between S-BN and water favored the surface reaction, which may be one of the factors for the higher photocatalytic activity of S-BN.

To investigate the photocatalytic activities of *h*-BN and S-BN, 2,4-DCP was selected as the target pollutant to test the degradation effect under different light condition. Before the degradation experiments, the absorption ability of *h*-BN and S-BN was measured (Figure S11). Obviously, both *h*-BN and S-BN could reach adsorption equilibrium within 30 min, indicating that the dark reaction for 30 min can remove the influence of adsorption on the degradation efficiency in the degradation experiments. As shown in Fig. 5a, the S-BN samples show enhanced photocatalytic activities under UV light irradiation compared with *h*-BN. The improved photocatalytic performance came from the synthetic action of enhanced optical absorption, charge transfer and surface reactivity. And when exposed to visible light, pristine *h*-BN showed little photocatalytic activities due to its wide bandgap, while about 77% of 2,4-DCP could be removed in 60 min over S-BN, indicating the introduction of S can expand the light utilization to the

visible region. To study the mineralization ability of *h*-BN and S-BN, the TOC removal rate was measured and shown in Figure S12. The S-BN photocatalyst can remove about 73% and 47% of TOC in 60 min under UV light and visible light, respectively, which were much higher than the *h*-BN samples (TOC remove rates about 41% and 13% under UV and visible light). In addition, scavenge experiments (Fig. 5b) proved that the photoinduced holes (h^+) and hydroxyl radical ($\cdot OH$) played a major role in the degradation process as oxidative species, and the weak inhibitory effect of 1,4-benzoquinone suggests the small contribution of superoxide radical ($\cdot O_2^-$) on the 2,4-DCP degradation. Also, the ESR (electron spin resonance) spin-trap technology based on S-BN was performed to confirm the existence of OH and $\cdot O_2^-$. As shown in Fig. 5c, both the characteristic signals of DMPO-OH and DMPO- $\cdot O_2^-$ can be observed, indicating the existence of these two active species in the reaction system. However, at the same illumination time (10 min), the signal intensity of DMPO-OH is much stronger than DMPO- $\cdot O_2^-$, suggesting that the OH was the major reactive radical in the degradation process, and the $\cdot O_2^-$ only played a minor role. The reusability test of S-

BN was performed and revealed its excellent stability with negligible activity reduction after three runs (Fig. 5d). The XRD patterns of pristine and recycled S-BN (Figure S13) were measured and suggested the high stability and well-preserved crystalline structure of samples. Based on all of the above characterization and experimental results, a possible charge transfer and photocatalytic mechanism is proposed and illustrated in Fig. 5e. After the introduction of S, the d-orbitals of S atoms participated in the composition of VB and caused the downwards of VB position, which effectively enhanced the optical absorption capability of h-BN. Moreover, the increased interlayer interaction caused by S doping could compress the interlayer stacking distance, which was beneficial for the interlayer charge transfer. When S-BN was exposed to light irradiation, photogenerated charges could be excited and migrate to the surface through the interlayer transfer. The holes on the VB of S-BN exhibited strong oxidation activity that could directly react with pollutants or oxidize water into OH [55,56], while the electrons on the CB of S-BN could only produce limited O₂⁻ due to the low CB potential. Hence, the organic pollutants (2,4-DCP) could be damaged and degraded under the synergistic effect of h⁺, OH and O₂⁻.



4. Conclusions

In summary, we demonstrated a facile and robust strategy to achieve sulfur doping of h-BN through two-step thermal treatment, and the doping amounts of sulfur can be controlled by changing the heat treatment duration. It was found that the doping of sulfur can compress the layer spacing of h-BN and shorten the bandgap, and the variation can be adjusted by controlling the amount of sulfur contents within a certain range. The compressed interlayer spacing results in enhanced charge transfer capacity, and the narrowing of bandgap enhances the photo-absorption ability and exhibits a redshift in the absorption edge of h-BN to visible region. We also studied the band structure of h-BN and S-BN through the DFT calculations, and revealed the relationship between the band structure changing and sulfur doping at the atomic orbital level. The hybridization of S atomic orbitals leads to the formation of new valence and conduction band, thus results in the narrowed bandgap. In addition, the prepared S-BN samples also exhibit enhanced surface reactivity and hydrophilicity, which is beneficial for the photocatalytic performance of h-BN in the treatment of waste water. The 2,4-DCP degradation experiments confirmed that the prepared S-BN not only exhibited enhanced photocatalytic activity under UV light, but also showed great removal effect on 2,4-DCP under visible light. We hypothesize that the facile strategy could provide directions for the preparation and modification of h-BN-based photocatalytic materials or other 2D semiconductors for improved solar energy capture and conversion.

Acknowledgments

The study was financially supported by Projects 51579096, 51521006 and 51222805 supported by National Natural Science Foundation of China, the Key Research and Development Program of Hunan Province of China (2017SK2241), the National Innovative Talent Promotion Program of China (2017RA2088), and the National Program for Support of Top-Notch Young Professionals of China (2012). The authors would like to thank the support from Hunan Province Cooperative Innovation Center for The Construction & Development of Dongting Lake Ecological Economic Zone.

Appendix A. Supplementary data

Supplementary material related to this article can be found, in the online version, at doi:<https://doi.org/10.1016/j.apcatb.2019.117827>.

References

- [1] Y. Fang, X. Wang, *Angew. Chemie Int. Ed. Engl.* 56 (2017) 15506–15518.
- [2] M.Z. Ghori, S. Veziroglu, B. Henkel, A. Vahl, O. Polonsky, T. Strunskus, F. Faupel, O.C. Aktas, *Sol. Energy Mater. Sol. Cells* 178 (2018) 170–178.
- [3] A. Prakash, M. Dan, S. Yu, S. Wei, Y. Li, F. Wang, Y. Zhou, *Sol. Energy Mater. Sol. Cells* 180 (2018) 205–212.
- [4] M. Zhou, P. Yang, S. Wang, Z. Luo, C. Huang, X. Wang, *ChemSusChem* 11 (2018) 3949–3955.
- [5] Y. Deng, L. Tang, G. Zeng, Z. Zhu, M. Yan, Y. Zhou, J. Wang, Y. Liu, J. Wang, *Appl. Catal. B-Environ.* 203 (2017) 343–354.
- [6] J. Wang, L. Tang, G. Zeng, Y. Deng, Y. Liu, L. Wang, Y. Zhou, Z. Guo, J. Wang, C. Zhang, *Appl. Catal. B-Environ.* 209 (2017) 285–294.
- [7] J. Wang, L. Tang, G. Zeng, Y. Deng, H. Dong, Y. Liu, L. Wang, B. Peng, C. Zhang, F. Chen, *Appl. Catal. B-Environ.* 222 (2018) 115–123.
- [8] Y. Deng, L. Tang, C. Feng, G. Zeng, J. Wang, Y. Lu, Y. Liu, J. Yu, S. Chen, Y. Zhou, *ACS Appl. Mater. Inter.* 9 (2017) 8349.
- [9] M. Zheng, J. Shi, T. Yuan, X. Wang, *Angew. Chemie Int. Ed. English* 57 (2018) 5487–5491.
- [10] C. Tan, X. Cao, X.J. Wu, Q. He, Y. Jian, Z. Xiao, J. Chen, Z. Wei, S. Han, G.H. Nam, *Chem. Rev.* 117 (2017) 6225.
- [11] R. Dong, M. Pfeffermann, H. Liang, Z. Zheng, X. Zhu, J. Zhang, X. Feng, *Angew. Chemie Int. Ed. English* 54 (2015) 12058–12063.
- [12] N. Yang, J. Zhai, D. Wang, Y. Chen, L. Jiang, *ACS Nano* 4 (2010) 887–894.
- [13] J. Zhu, P. Wei, J. Key, S. Yin, S. Ma, P.K. Shen, *Sustain. Energy Fuels* 3 (2019) 478–487.
- [14] B.W. Baugher, H.O. Churchill, Y. Yang, P. Jarilloherrero, *Nat. Nanotechnol.* 9 (2014) 262.
- [15] B. Peng, L. Tang, G. Zeng, S. Fang, X. Ouyang, B. Long, Y. Zhou, Y. Deng, Y. Liu, J. Wang, *Biosens. Bioelectron.* 121 (2018) 19–26.
- [16] D. Xu, B. Cheng, W. Wang, C. Jiang, J. Yu, *Appl. Catal. B-Environ.* 231 (2018) 368–380.
- [17] L. Tang, C. Feng, Y. Deng, G. Zeng, J. Wang, Y. Liu, H. Feng, J. Wang, *Appl. Catal. B-Environ.* 230 (2018) 102–114.
- [18] J. Chen, X.J. Wu, L. Yin, B. Li, X. Hong, Z. Fan, B. Chen, C. Xue, H. Zhang, *Angew. Chemie Int. Ed. English* 54 (2015) 1210.
- [19] Y. Deng, L. Tang, C. Feng, G. Zeng, J. Wang, Y. Zhou, Y. Liu, B. Peng, H. Feng, J. Hazard. Mater. 344 (2017) 758–769.
- [20] Q. Zhang, Z. Li, S. Wang, R. Li, X. Zhang, Z.X. Liang, H. Han, S. Liao, C. Li, *ACS Catal.* 6 (2016) 2182–2191.
- [21] G. Xi, S. Ouyang, P. Li, J. Ye, Q. Ma, N. Su, H. Bai, C. Wang, *Angew. Chemie Int. Ed. English* 124 (2012) 2445–2449.
- [22] F. Cheng, H. Wang, X. Dong, *Chem. Commun. (Camb.)* 51 (2015) 7176–7179.
- [23] Yang Guidong, *Appl. Catal. B-Environ.* 198 (2016) 276–285.
- [24] N. Meng, J. Ren, Y. Liu, Y. Huang, T. Petit, B. Zhang, *Synth. Lect. Energy Environ. Technol. Sci. Soc.* 11 (2018) 566–571.
- [25] Q. Han, Z. Cheng, B. Wang, H. Zhang, L. Qu, *ACS Nano* 12 (2018) 5221–5227.
- [26] G. Zhang, G. Li, Z.A. Lan, L. Lin, A. Savateev, T. Heil, S. Zafeiratos, X. Wang, M. Antonietti, *Angew. Chemie Int. Ed. English* 129 (2017) 1–6.
- [27] J. Cheng, Z. Hu, K. Lv, X. Wu, Q. Li, Y. Li, X. Li, J. Sun, *Appl. Catal. B-Environ.* 232 (2018) 330–339.
- [28] L. Jiang, X. Yuan, G. Zeng, Z. Wu, J. Liang, X. Chen, L. Leng, H. Wang, H. Wang, *Appl. Catal. B-Environ.* 221 (2017) 715–725.
- [29] W. Lei, D. Portehault, D. Liu, S. Qin, Y. Chen, *Nat. Commun.* 4 (2016) 1777.
- [30] C. Zhou, C. Lai, C. Zhang, G. Zeng, D. Huang, M. Cheng, L. Hu, W. Xiong, M. Chen, J. Wang, *Appl. Catal. B-Environ.* 238 (2018) 6–18.
- [31] S. Ding, D. Mao, S. Yang, F. Wang, L. Meng, M. Han, H. He, C. Sun, B. Xu, *Appl. Catal. B-Environ.* 210 (2017) 386–399.
- [32] J. Di, J. Xia, M. Ji, B. Wang, Y. Sheng, Z. Qi, Z. Chen, H. Li, *Appl. Catal. B-Environ.* 183 (2016) 254–262.
- [33] Z. He, C. Kim, L. Lin, T.H. Jeon, S. Lin, X. Wang, W. Choi, *Nano Energy* 42 (2017) 58–68.
- [34] C. Huang, C. Chen, M. Zhang, L. Lin, X. Ye, S. Lin, M. Antonietti, X. Wang, *Nat. Commun.* 6 (2015) 7698.
- [35] L. Chen, X. Wang, *Chem. Commun.* 53 (2017) 11988–11991.
- [36] L. Chen, M. Zhou, Z. Luo, M. Wakeel, A.M. Asiri, X. Wang, *Appl. Catal. B-Environ.* 241 (2019) 246–255.
- [37] Z. Luo, Y. Fang, M. Zhou, X. Wang, *Angew. Chemie Int. Ed. English* 58 (2019) 6033–6037.
- [38] M. Zhou, S. Wang, P. Yang, C. Huang, X. Wang, *ACS Catal.* 8 (2018) 4928–4936.
- [39] Q. Weng, Y. Ide, X. Wang, X. Wang, C. Zhang, X. Jiang, Y. Xue, P. Dai, K. Komaguchi, Y. Bando, *Nano Energy* 16 (2015) 19–27.
- [40] Q. Weng, D.G. Kvashnin, X. Wang, O. Cretu, Y. Yang, M. Zhou, C. Zhang, D.M. Tang, P.B. Sorokin, Y. Bando, *Adv. Mater.* 29 (2017) 1700695.
- [41] Y. Cao, P. Maitarad, M. Gao, T. Taketsugu, H. Li, T. Yan, L. Shi, D. Zhang, *Appl. Catal. B-Environ.* 238 (2018) 51–60.
- [42] L. Wang, S.Q. Ni, C. Guo, Y. Qian, *J. Mater. Chem. A Mater. Energy Sustain.* 1 (2013) 6379–6387.
- [43] Z. Chen, T. Fan, M. Shao, X. Yu, Q. Wu, J. Li, W. Fang, X. Yi, *Appl. Catal. B-Environ.*

242 (2019) 40–50.

[44] L. Tang, C. Feng, Y. Deng, G. Zeng, J. Wang, Y. Liu, H. Feng, J. Wang, *Appl. Catal. B-Environ.* 230 (2018) 102–114.

[45] Y. Deng, L. Tang, G. Zeng, J. Wang, Y. Zhou, J. Wang, L. Wang, C. Feng, J. Colloid. Interf. Sci. 509 (2017) 219–234.

[46] C. Feng, Y. Deng, L. Tang, G. Zeng, J. Wang, J. Yu, Y. Liu, B. Peng, H. Feng, J. Wang, *Appl. Catal. B-Environ.* 239 (2018) 525–536.

[47] L. Wang, X. Duan, G. Wang, C. Liu, S. Luo, S. Zhang, Y. Zeng, Y. Xu, Y. Liu, X. Duan, *Appl. Catal. B-Environ.* 186 (2016) 88–96.

[48] H.J. Kong, H.W. Da, J. Kim, S.I. Woo, *Chem. Mater.* 28 (2016) 1318–1324.

[49] Z. Hu, Z. Shen, J.C. Yu, *Chem. Mater.* 28 (2016) 564–572.

[50] Z. Jiang, H. Sun, T. Wang, B. Wang, W. Wei, H. Li, S. Yuan, T. An, H. Zhao, J. Yu, *Synth. Lect. Energy Environ. Technol. Sci. Soc.* 11 (2018) 2382–2389.

[51] C. Liu, H. Huang, L. Ye, S. Yu, N. Tian, X. Du, T. Zhang, Y. Zhang, *Nano Energy* 41 (2017) 738–748.

[52] G. Liu, J. Shi, F. Zhang, Z. Chen, J. Han, C. Ding, S. Chen, Z. Wang, H. Han, C. Li, *Angew. Chemie Int. Ed. English* 53 (2014) 7295–7299.

[53] J.C. Hill, A.T. Landers, J.A. Switzer, *Nat. Mater.* 14 (2015) 1150.

[54] X. Jiao, Z. Chen, X. Li, Y. Sun, S. Gao, W. Yan, C. Wang, Q. Zhang, Y. Lin, Y. Luo, J. Am. Chem. Soc. 139 (2017) 7586.

[55] T. Chen, Q. Zhang, Z. Xie, C. Tan, P. Chen, Y. Zeng, F. Wang, H. Liu, Y. Liu, G. Liu, W. Lv, *Appl. Catal. B-Environ.* 238 (2018) 410–421.

[56] Q. Zhang, P. Chen, M. Zhuo, F. Wang, Y. Su, T. Chen, K. Yao, Z. Cai, W. Lv, G. Liu, *Appl. Catal. B-Environ.* 221 (2018) 129–139.